Arch. Metall. Mater. **70** (2025), 2, 663-671

DOI: https://doi.org/10.24425/amm.2025.153467

ZHONGYAO LI[1,2], LI FENG[3], JIANJUN GUAN[1], YAN ZHAO[1*],
YANHONG YANG[2*], JIAOJIAO ZHU[1]

TUNGSTEN ARGON ARC WELDING CRACK ANALYSIS AND NUMERICAL SIMULATION FOR RESIDUAL STRESS OF Co-BASED SUPERALLOY

The influence of welding current decay time on the repair of Co-based superalloy by tungsten argon arc welding spot welding are investigated by means of simulation and experiments. The results show that: the maximum tensile stress of residual stress after welding is distributed in the center area, gradually decreases towards the edge area, and mainly exists in the form of compressive stress in the edge area. On the same welding current, with the increase of attenuation time, the overall trend of temperature and stress distribution, and the stress value increases. The larger the fusion zone (FZ) crack area and the smaller intergranular cracks in the heat affected zone (HAZ) decrease. Currently, there is limited research on the influence of welding current decay time on the repair of Co-based superalloys via tungsten argon arc spot welding.

Keywords: Finite element method; argon tungsten arc welding; postweld crack; cobalt base superalloy

1. Introduction

With the rapid development of the aerospace industry, numerous researchers have been devoted to the development of alloys that exhibit improved performance and are more suited to this field [1-2]. Due to the exceptional high-temperature properties of superalloy, the research and development of novel superalloy is closely associated with the advancements in the aerospace sector [3]. Co-based superalloys are widely used in turbine blades of engines but, these components can suffer from different degrees of damage such as wear and corrosion, leading to a decline in performance [4-6]. Instead of replacing these costly parts, repairing the damaged or degraded areas is a more economical option. Welding is a commonly used method for repairing cracks in Co-based superalloys, as it is cost-effective and can provide comparable quality and integrity for the components [7]. Tungsten argon arc welding (TIG) is a primary technique utilized for the welding repair of superalloys [8-9]. One of the main challenges in the welding repair process is the occurrence of welding cracks. These cracks can directly or indirectly affect the performance of the components, and even tiny cracks that cannot be detected may become a potential cause of safety accidents [10-12].

The main reason for welding cracks is the presence of residual stress that cannot be eliminated during welding [13-14]. Understanding the distribution of residual stress after welding is vital for comprehending the mechanical properties of the welded parts. However, the traditional experimental approach for studying residual stress is time-consuming, expensive, and may yield less accurate data [15]. Finite element technology, along with various simulation software, has been constantly evolving [16-17], offering an alternative approach to study residual stress distribution after welding. By combining simulation techniques with experimental data, the research and development process can be expedited, while reducing costs [18-24].

It is important to note that the welding processes can have great effects on the repaired materials. Inappropriate selection of welding parameters can potentially compromise the components and lead to irreversible consequences. In this study, the influence of current attenuation time in the TIG welding process on welding cracks in the alloy is investigated using a combination of simulation and experiment. The temperature field and distribution of residual stress during the welding process are evaluated using ANSYS software.

[1] LIAONING PETROCHEMICAL UNIVERSITY, SCHOOL OF MECHANICAL ENGINEERING, FUSHUN 113001, CHINA
[2] CHINESE ACADEMY OF SCIENCES, SHI-CHANGXU INNOVATION CENTER FOR ADVANCED MATERIALS, INSTITUTE OF METAL RESEARCH, SHENYANG 110016, CHINA
[3] SHENGYANG POLYTECHNIC COLLEGE, ELECTRICAL ENGINEERING, SHENYANG 110045, CHINA

* Corresponding authors: zhaoyan@lnpu.edu.cn; yhyang@imr.ac.cn

© 2025. The Author(s). This is an open-access article distributed under the terms of the Creative Commons Attribution License (CC-BY 4.0). The Journal license is: https://creativecommons.org/licenses/by/4.0/deed.en. This license allows others to distribute, remix, modify, and build upon the author's work, even commercially, as long as the original work is attributed to the author.

2. Experiment method

2.1. Experiment parameter

The welding experiments in this study utilized cylindrical Co-based superalloy flakes with a diameter of 16 mm and a thickness of 2 mm. Tungsten argon arc spot welding was the chosen welding method, with a duration of 3 seconds, an arc length of 1 mm, and a welding current of 25 A. Two different conditions were tested, with controlled current decay times of 0 s and 4 s.

2.2. Finite element method

ANSYS software was used for numerical simulation of welding residual stress. In order to ensure the accuracy results, the model ratio was one to one according to the shape (thin cylindrical) and size ($\phi 16 \times 2$ mm) in welding part. For mesh division, the mapping mesh partition method was utilized, which proved to be more suitable in terms of shape and quality compared to other methods. The ANSYS simulation employed the mapping mesh division method to generate polyhedral mesh on the body.

In practical welding processes, the heat input and temperature distribution in the welding parts are non-uniform. The heat is higher concentrated in welding heat source, so the temperature of the welding center area and its vicinity is higher. As the distance from the heat source increases, the heat and temperature rapidly decrease. The grid of the weld and nearby area should be divided into a fine and neat point to ensure the relative accuracy of calculation.

The finite element model is established according to the entity of weldment. The mesh division is based on the actual situation of non-uniform mesh division. In the fusion zone and heat affected zone of the molten pool, a close regular quadrilateral grid is adopted, and a sparse and irregular grid is used in the far region. The final result of finite element meshing is shown in Fig. 1. The total number of meshing cells is 3696, and the number of nodes is 3063.

The welding method in the paper is GTAW spot welding. According to the actual welding situation, the welding heat source model selected is Gaussian heat source model. The effective arc radius of Gaussian heat source model is 0.006. The specific heat flow at any point on the heating center is shown in Formula 1.

$$Q_R = Q_0 \exp\left(-\frac{3r^2}{r_0}\right) \tag{1}$$

Where Q_R represents the surface heat flow at r; Q_0 represents the maximum heat flow density at the heating center; r_0 represents effective arc heating radius (m); r stands for distance to arc heating center (m).

Considering the complexity and computation of welding process, some initial conditions are simplified. The ambient temperature is room temperature (25°C), and the thermophysical properties of the materials were assumed to vary with temperature. The thermophysical properties of the materials used in the model are shown in TABLE 1.

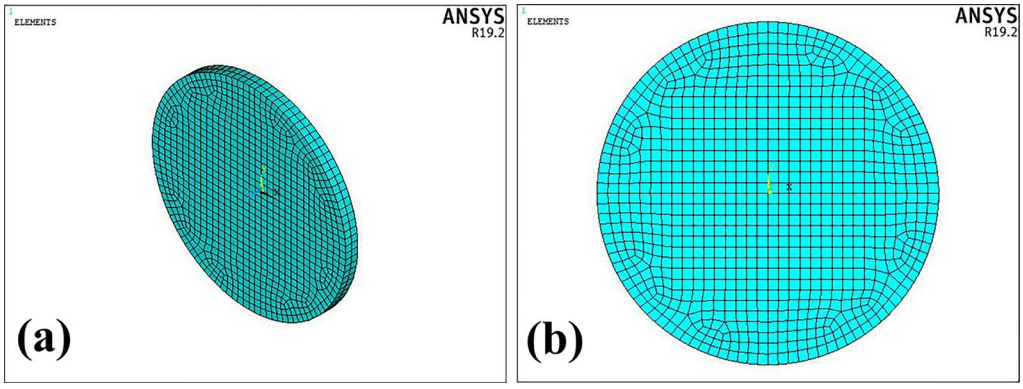

Fig. 1. ANSYS (a) finite model (b) front view of finite model

TABLE 1

Thermophysical performance parameters

Temperature, °C	Density, kg/m^3	Specific heat, J/kg·°C	Thermal conductivity, W/m·°C	Poisson's ratio	Elastic moduli, GPa	Thermal expansivity, I/°C	Yield strength, MPa
25	8190	425.5	11.4	0.3	271	1.25 e^{-5}	460
400	8043	525	17.5	0.3	221	1.4 e^{-5}	449
600	7964.6	580	20.5	0.3	209	1.45 e^{-5}	438
800	7886.2	630	23.4	0.3	151	1.5 e^{-5}	427
1200	7729.4	721	30.5	0.3	111	1.65 e^{-5}	99.8
1500	7255.7	810	35.1	0.3	100	1.75 e^{-5}	5
3000	5935.7	1080	57.2	0.3	100	1.75 e^{-5}	5

3. Results and discussion

The molten pool formed during Tungsten Inert Gas (TIG) welding consists of three distinct regions: the base material, fusion zone, and heat-affected zone. The fusion line marks the boundary between the fusion zone and the heat-affected zone. The morphology after GTAW spot welding is shown in Fig. 2(a), and the morphology of the molten pool is marked. Fig. 2(b) is a schematic diagram of the post-weld pool, which includes base metal zone (BM), fusion zone (FZ), heat affected zone (HAZ) and fusion line.

3.1. Effect of current decay time on molten pool morphology

Fig. 3 shows the contrast morphology of welding molten pool under the condition of spot welding time 3 s, welding current 25 A, different dacay time 0 s and 4 s. For the characteristics of fusion zone morphology, as shown in Fig. 3(a) and (b), it can be observed that the cracks extending in the transverse and longitudinal directions are more pronounced at the intersection with a decay time of 4 s compared to 0 s. It is similar to the intersection of cracks in three large directions. The crack length increases significantly as shown in Fig. 4. As the decay time increases, so does the heat input to the weldment. It can also be seen from Fig. 5 that when the welding current decay time is 4 s, the molten pool area also increases significantly. The error bars in Figs. 4 and 5 were determined based on two sets of experiments conducted for each parameter. This approach was adopted to enhance the scientific rigor and accuracy of the experimental results. The influence of welding decay time of 0 s on the morphology of the heat-affected zone is shown in Fig. 3(c), and obvious fine cracks along the grain can be observed. Fig. 3(d) express that the fine cracks in the intergranular cracking of the heat affected zone are not as obvious as those in the case of 0 s. These fine intergranular cracks tend to decrease with the increase of welding decay time.

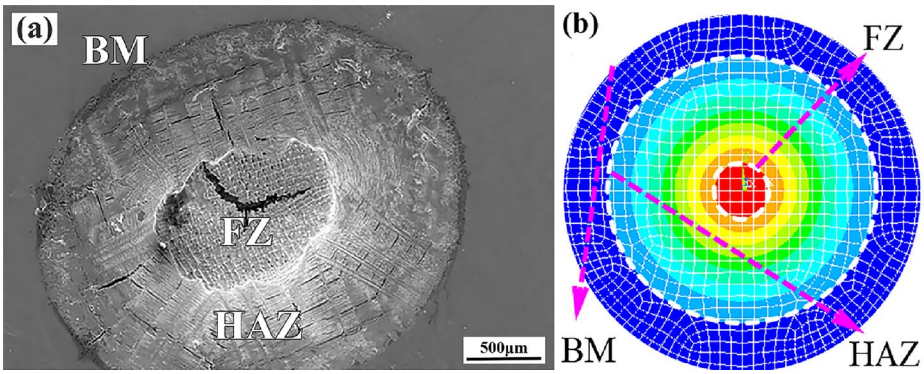

Fig. 2. (a) Morphology of molten pool (b) Regional distribution of BM, HAZ and FZ in numerical simulat

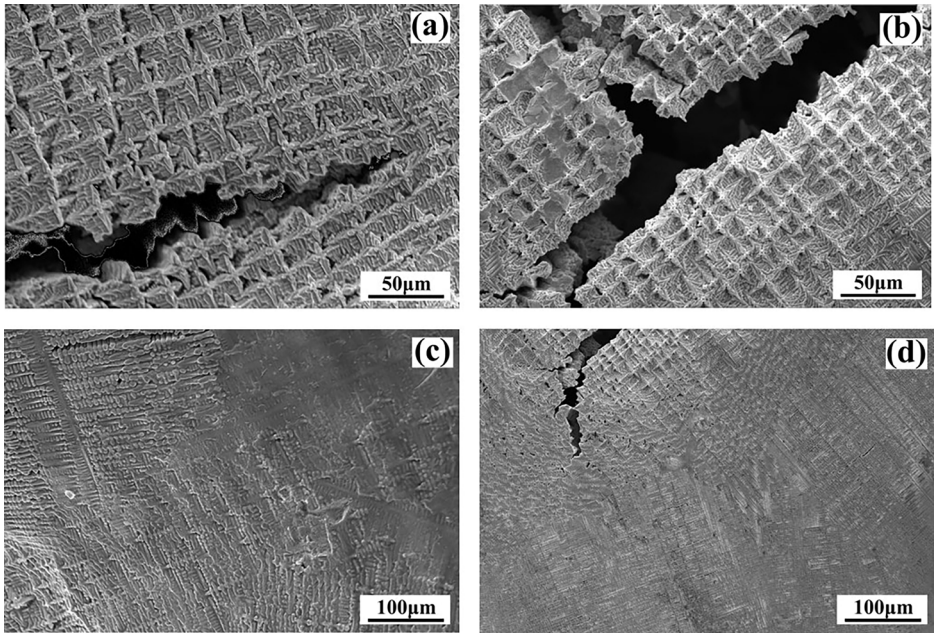

Fig. 3. Morphology of molten pool after welding, welding current with 25 A and decay times with 0 s and 4 s, (a) 0 s, FZ (b) 4 s, FZ (c) 0 s, HAZ (d) 4 s, HAZ

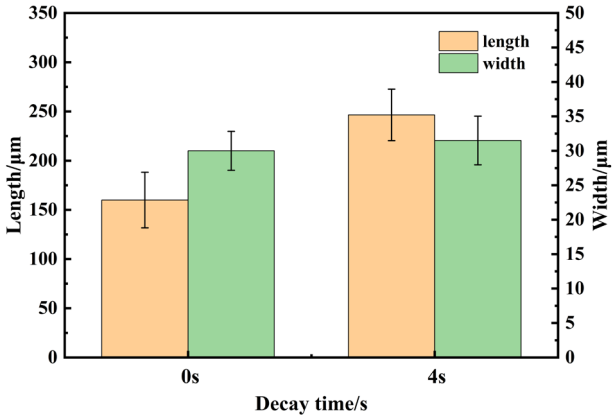

Fig. 4. Distribution of welding crack length and width under different decay time, (a) 0 s, (b) 4 s

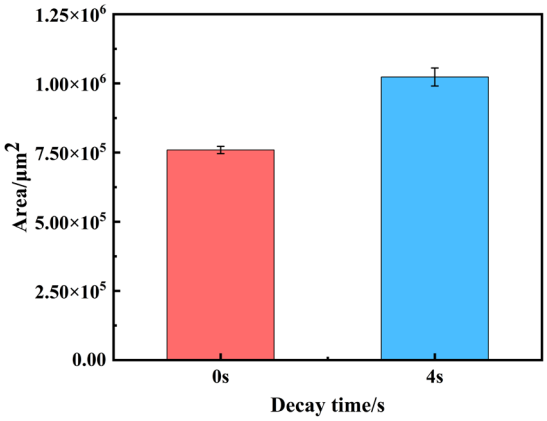

Fig. 5. Distribution of weld pool area after welding with different decay time, (a) 0 s, (b) 4 s

3.2. Numerical simulation of temperature field

The distribution cloud diagram of temperature field of weldment at different time points in the welding process is shown in Fig. 6. Fig. 6(a)-(b) is the cloud diagram of the heating stage of welding process, and Fig. 6(c)-(f) is the welding cooling process. The heating and cooling process of welding, the dynamic change of the whole temperature field could be clearly observed.

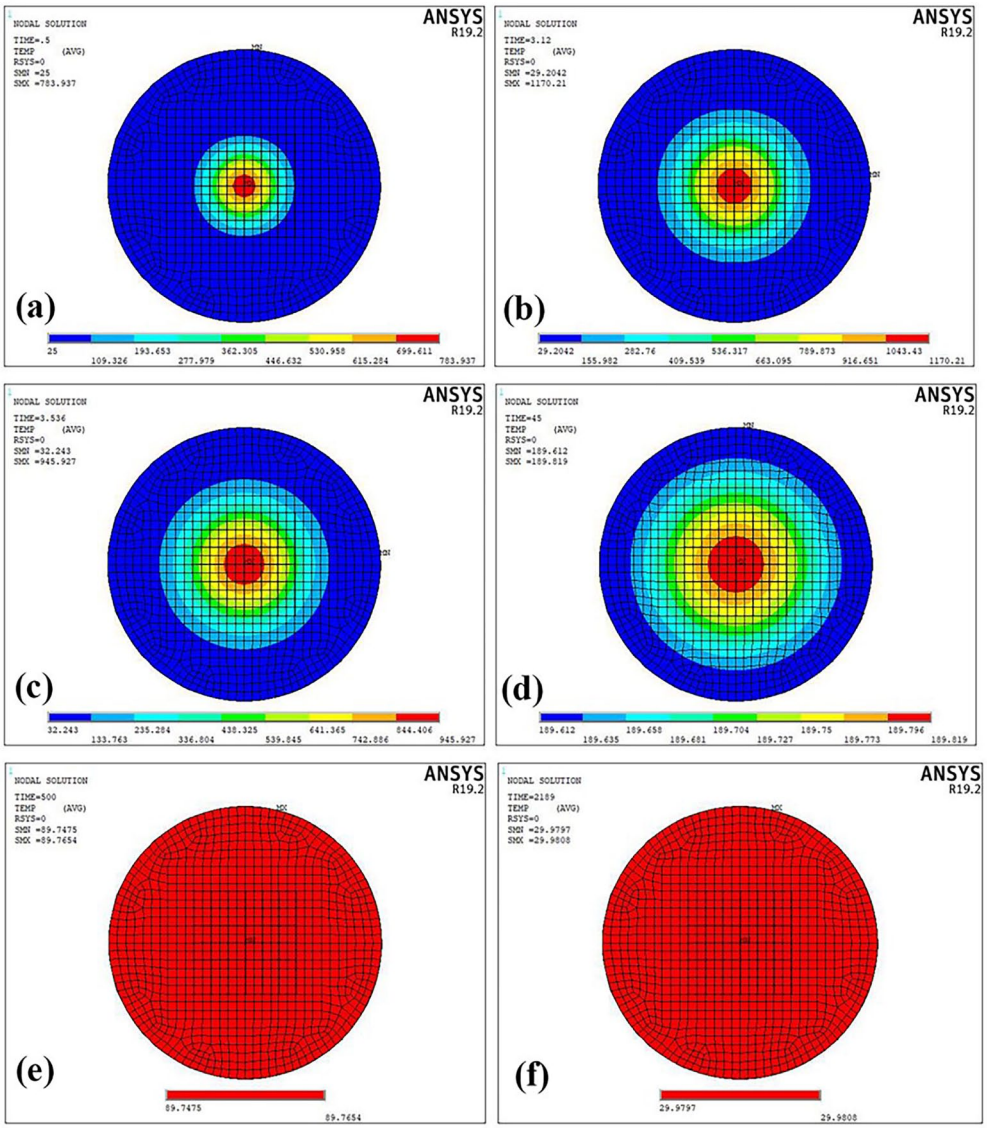

Fig. 6. Cloud map of temperature field distribution of weldment at different time points, (a) 0.5 s, (b) 3.12 s, (c) 3.54 s, (d) 45 s, (e) 500 s, (f) 2189 s

At different time points, the temperature of welding parts at different time points changes. During the heating stage, as shown in Fig. 6(a)-(b), the temperature of the welding parts increases rapidly, resulting in an uneven distribution of the temperature field with a significant temperature gradient. The isotherms appear dense at the front end of the weld pool. Moving on to the cooling process, as shown in Fig. 6(c)-(f), a relatively stable temperature field is formed on the welded parts over time.

The distribution cloud diagram at 0.5 seconds is shown in Fig. 6(a). In the diagram, we observed that the distribution trend was very uneven and there was a large temperature difference. The central region exhibits a high temperature with a small area, reaching 783.94℃ at the center of the molten pool. The cloud image of temperature field distribution at 3.12 seconds is shown in Fig. 6(b), the distribution of temperature field is wider than 0.5 seconds and the temperature gradient is very large, with the temperature in the center of the molten pool reaches 1170.21℃. The cloud diagram of temperature field distribution at 3.54 seconds is shown in Fig. 6(c), the distribution of temperature field is larger than 3.12 seconds and the temperature gradient is very large. The temperature in the center of the molten pool reaches 945.93℃. The cloud diagram of temperature field distribution at 45 seconds is shown in Fig. 6(d), the distribution of temperature field is further expanded than 3.54 seconds, the temperature gradient is relatively uniform. The temperature in the center of the molten pool reaches 189.82℃. The temperature field distribution cloud at 500 seconds is shown in Fig. 6(e), the temperature field near the molten pool becomes consistent, with a temperature of 89.75℃. The distributed cloud diagram at 2189 seconds is shown in Fig. 6(f), the temperature in and around the molten pool becomes uniform, measuring 29.98℃.

Throughout the entire welding process, the welding parts undergo heating and cooling processes, and the temperature increases rapidly with the increase of time in the heating process. The temperature is high in the center of the molten pool, and then decreases continuously toward the edge area, resulting in a significant temperature gradient. During the cooling process, the temperature gradually decreases with the increase of time, the temperature gradient is roughly the same after a certain time. The temperature near the molten pool becomes consistent with the remote area. In this paper, only one of the welding parameters, the temperature field distribution cloud diagram when the welding current is 25 A and the decay time is 0 s, is shown in Fig. 6. The temperature field cloud diagram with decay time of 4 s is not shown, but the law of calculation results and analysis results is consistent.

The temperature at different time points in the temperature field of 0 s and 4 s of welding current 25 A is shown in Fig. 7. It can be seen that the calculation results of the finite elemcess, there is a noteworthy consistency among the temperature curves of individual points located along the center line of the weldment, the prominent occurrence of maximum temperature at the central region of the weld pool. With the progression of time, a quasi-steady state field emerges at a specific moment, aligning with the numerical simulation outcomes, which further indicates that the setting of heat source grid and grid division in the model is reasonable, and is consistent with the actual welding situation.

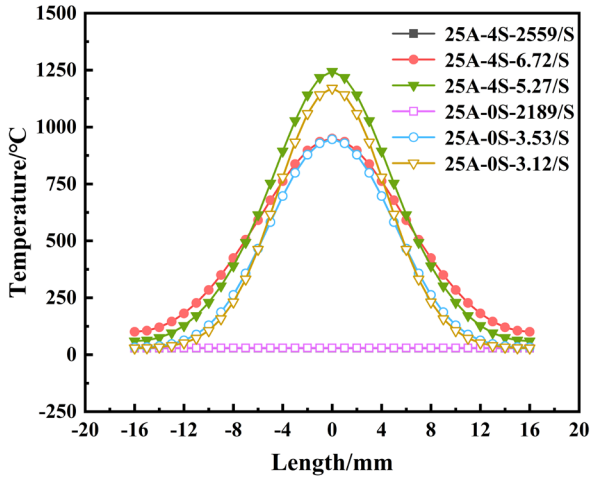

Fig. 7. Temperature time history diagram

3.3. Numerical simulation of stress field

Upon the application of an external force, the material undergoes a certain degree of deformation, which subsequently reverts back to its original state upon the removal of the external force. The deformation induced by the external force is referred to as elastic strain. Plastic strain is also known as permanent deformation, which denotes the irreversible deformation that occurs under the influence of stress. Upon the removal of stress, there remains a residual strain that cannot be completely eliminated within the material. Fig. 8 express the curves of elastic strain and plastic strain when welding current is 25 A and decay time is 0 s and 4 s. It is observed that for a decay time of 0 s, the elastic strain curve exhibits a compressive stress in the time range of 0 s to 3.12 s, transitioning into a tensile stress thereafter at 3.12 s. The tensile stress reaches its peak at 3.54 s. The plastic strain curve reaches its lowest value at 3 s. When the decay time is 4 s,

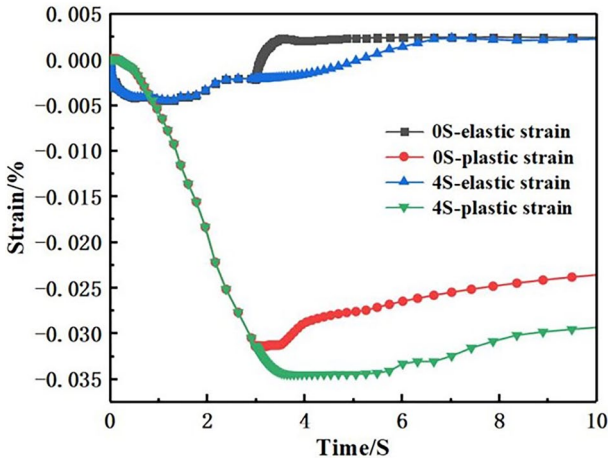

Fig. 8. Elastoplastic strain distribution diagram at welding current of 25 A

the elastic strain curve is compressive stress at 0 s-5.27 s and becomes tensile stress at 5.27 s. The tensile stress reaches its peak at 7.04 s. The plastic strain curve reaches its lowest value at 3.71 s.

The stress along the weld is usually referred to as the longitudinal stress, denoted by σ_x. The stress perpendicular to the direction of the weld, called the transverse stress, is expressed by σ_y. The cooling rates on the surface and inside of the weldment are different. If the thickness of the weldment is large, there is also stress in the thickness direction of the weldment, which is expressed by σ_z. In the fabrication of welded structures, the dimensions of the material employed, in terms of length and width, are typically larger than the thickness. In the case of thin plates with a thickness less than 20 mm, the resulting welding stress in the direction perpendicular to the plate thickness is considered to be negligible, thus exhibiting plane stress conditions. Significant residual stress only arises in the direction of thickness for large or very large welded structures. The weldment thickness in this paper is merely 2 mm, making the primary focus of this study center around the analysis and comparison of plane stress conditions.

After the calculation of the stress field, the typical stress field distribution in the welding process can be observed. As shown in Fig. 9, The distribution cloud diagram of the longitudinal stress field at the welding current 25 A decay time of 0 s is shown in Fig. 9(b). It can be observed that the residual stress σ_x is 812 MPa. The distribution cloud diagram of transverse stress σ_y stress field at the welding current 25 A decay time of 0S is shown in Fig. 9(c). It can be observed that σ_y residual stress is 812 MPa. The distribution of longitudinal stress σ_x and transverse stress σ_y at the decay time of welding current 25 A for 0s is shown in Fig. 9(d)(e). As can be seen from Fig. 9(d), longitudinal shrinkage occurs after welding, resulting

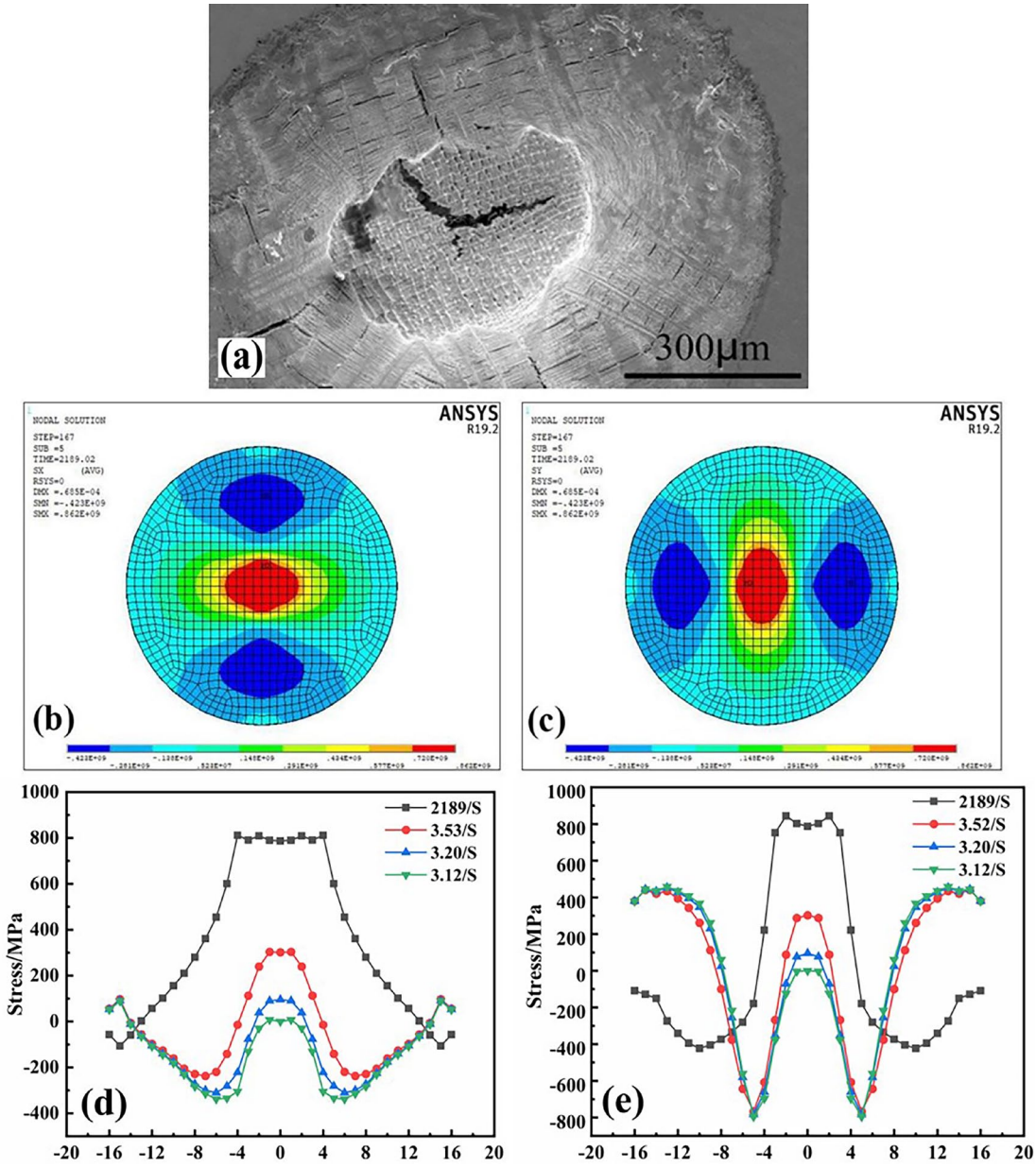

Fig. 9. Cracks produced when current is 25 A and decay time is 0 s, (a) Morphology of molten pool after welding, (b) and (c) Contour diagram of welding residual stress distribution, (d) and (e) Welding residual stress distribution curve

in longitudinal residual stress. The longitudinal residual stress within the weldment exhibits a tensile stress distribution in the central region, gradually transitioning to compressive stress and subsequently reverting to tensile stress as the distance from the center increases. The intermediate residual stress value can reach up to 812 MPa. The longitudinal residual stress in the middle tends to be stable within a certain range, and the stress in the edge tends to zero. By observing the following Fig. 9(e), it can be seen that near the center, the transverse residual stress within the weldment exhibits an approximate stress magnitude of 800 MPa, predominantly in the form of tensile stress. It subsequently transitions to compressive stress and then reverts to tensile stress, with the stress value approaching zero in the edge region. The morphology of the weld pool after welding when the welding current is 25 A and the decay time is 0 s is shown in Fig. 9(a). It can be observed that the data simulated by finite element is consistent with the test results. The simulated stress distribution reveals a gradual decrease in the maximum tensile stress of the fusion zone (FZ) as it extends towards the heat-affected zone (HAZ). Eventually, the stress value approaches zero at the base metal (BM). Based on the observations depicted in Fig. 9(a), prominent transverse and longitudinal cracking cracks are evident within the fusion zone (FZ), while the heat-affected zone (HAZ) exhibits localized intergranular cracking cracks of a finer nature. Minimal cracks are observed within the base metal (BM), thereby providing additional evidence to support the reasonableness and consistency of our simulation results when compared to experimental findings.

The vertical stress distribution cloud diagram σ_x of the welding current at 25 A decay time of 4 s is shown in Fig. 10(b). It can be observed that σ_x residual stress is 818 MPa. The transverse stress distribution cloud diagram σ_y when the welding

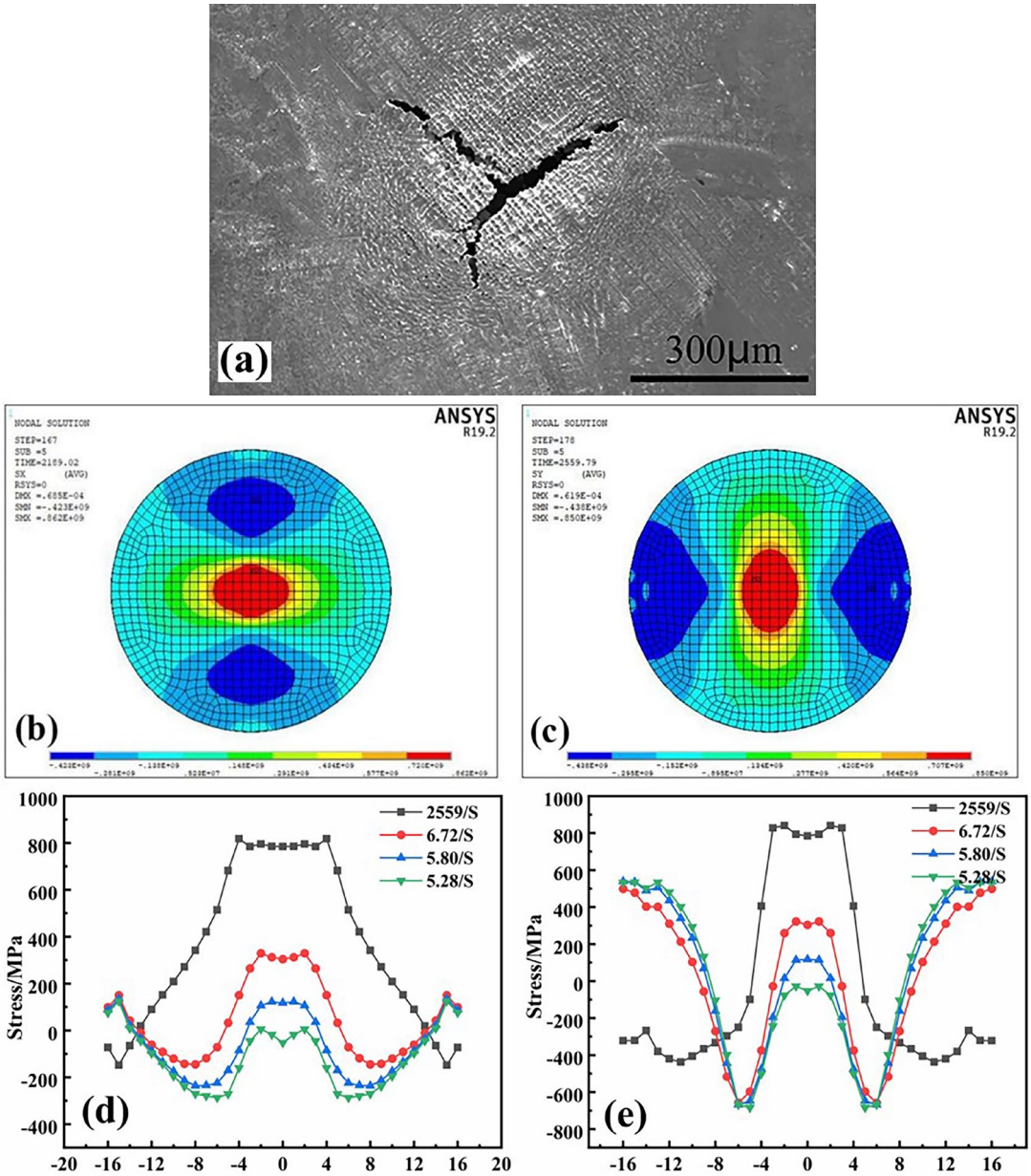

Fig. 10. Cracks produced when current is 25 A and decay time is 4 s, (a) Morphology of molten pool after welding, (b) and (c) Contour diagram of welding residual stress distribution, (d) and (e) Welding residual stress distribution curve

current is 25 A and the decay time is 4 s is shown in Fig. 10(c). It can be observed that σ_y residual stress is 818 MPa. The distribution of longitudinal stress σ_x and transverse stress σ_y at decay time 0 s and 4 s of welding current 25 A is shown in Fig. 10(d)-(e). As can be seen from the observation of Fig. 10(d), longitudinal shrinkage occurs after welding, resulting in longitudinal residual stress. Longitudinal residual stress σ_x presents tensile stress in the middle region, which gradually decreases to compressive stress as the distance from the center increases. The intermediate residual stress value can reach up to 818 MPa. The longitudinal residual stress within the central region tends to stabilize within a specific range and tends towards zero in the edge region. By observing Fig. 10(e) below, it can be seen that the transverse residual stress σ_y is near 800 MPa near the center. Primarily characterized by tensile stress, the longitudinal residual stress undergoes a transition to compressive stress and subsequently returns to tensile stress. Ultimately, the stress value tends towards zero in the edge region. The morphology of the weld pool after welding when the welding current is 25 A and the decay time is 4 s can be observed in Fig. 10(a), the fusion zone (FZ) exhibits prominent transverse and longitudinal cracking, whereas the heat-affected zone (HAZ) undergoes fine intergranular cracking. In contrast, the base metal (BM) shows minimal crack formation. The simulation results demonstrate a gradual decrease in the maximum tensile stress within the fusion zone (FZ) towards the direction of the heat-affected zone (HAZ). In the base metal (BM), the stress value decreases to zero, therefore confirming the conclusion that the current decay time is 0 s. Nevertheless, when the decay time is 4 s, a comparison of the stress distribution reveals that the residual stress value at 4 s is greater than that at 0 s. This observation further supports the notion that the length and width of cracks within the fusion zone (FZ) are larger at 4 s compared to those at 0 s. In addition, at a decay time of 4 s, the temperature is higher, indicating a larger heat input, and consequently, a lesser occurrence of fine intergranular cracks within the heat-affected zone (HAZ).

In their study of tungsten electrode argon arc welding of a novel cobalt-based high-temperature alloy, Abedi et al. [23] discovered that the grain boundary segregation of element B governs the crack sensitivity during the welding process. Additionally, a reduction in grain size contributes to improved resistance against heat-affected zone (HAZ) cracking in the alloy. Consequently, a novel pre-welding heat treatment was developed to mitigate HAZ cracking in cobalt-based high-temperature alloys. They further observed [24] that with an increase in welding rate, the central region of the fusion zone (FZ) transitions from a mixture of columnar and equiaxed grains to predominantly equiaxed grains, resulting in reduced cracking tendencies during the welding process.

Currently, research on repairing cobalt-based high-temperature alloys using tungsten electrode argon arc welding primarily focuses on specific regions within the welding process. In this study, the authors investigated the FZ, HAZ, and base metal (BM) regions, and examined changes in temperature and stress fields during the welding process with consideration to the often neglected parameter of welding current decay time. By studying these variations, the crack sensitivity and morphology under different conditions were determined.

The decay time of welding current in tungsten argon arc spot welding is a crucial aspect in the repair process of cobalt-based high-temperature alloy components. However, due to its tendency to be overlooked, studying the influence of welding current decay time during tungsten argon arc spot welding repair is imperative. A thorough understanding of the mechanisms underlying temperature and stress variations after tungsten argon arc spot welding can provide valuable guidelines for developing new repair strategies. Furthermore, effective control of crack formation can significantly enhance the quality of the repair.

4. Conclusions

(1) The morphology shows that with the increase of decay time, the heat input increases, the crack length and width in the fusion zone increase, and the fine cracks along the crystal in the heat affected zone decrease. There is no obvious crack in the base metal zone.

(2) Through the simulation analysis, it is concluded that the central area of the weldment is mainly tensile stress. As the distance from the center increases, the tensile stress slowly changes to the compressive stress, and the compressive stress is concentrated in the marginal region. The maximum tensile stress occurs in the fusion zone. The residual stress far away from the center is small, and the temperature distribution and stress value increase with the increase of current decay time.

(3) By comparing the morphology with the simulation results, it is found that they are consistent, which further proves the feasibility of the simulation experiment.

Acknowledgements

This work was supported by Basic scientific research projects of colleges and universities of Liaoning Provincial Department of Education (No. LJKMZ20220753), National Key R&D Program of China under Grant (No.2021YFB3700401).

REFERENCES

[1] Q. Sun, Z.Y. Chen, M. Li, et al., Structural Evolution of High-Performance Mn-Alloyed Thermoelectric Materials: A Case Study of SnTe. Small. **17** (25), 2100525 (2021). DOI: https://doi.org/10.1002/smll-202100525

[2] L.C. Yin, W.D. Liu, M. Li, et al., High carrier mobility and high figure of merit in the CuBiSe2 alloyed GeTe. Advanced Energy Materials **11** (45), 2102913 (2021). DOI: https://doi.org/10.1002/aenm-202102913

[3] Peter C. Gasson, The Superalloys: Fundamentals and Applications. The Aeronautical Journal **112**, 291 (2008). DOI: https://doi.org/10.1017/S0001924000087509

[4] J. Sato, T. Omori, K. Oikawa, I. Ohnuma, R. Kainuma, K. Ishida, Cobalt-Base High-Temperature Alloys. Science **312**, 90-91 (2006). DOI: https://doi.org/10.1126/science-1121738

[5] N. Baler, P. Pandey, K. Chattopadhyay, G. Phanikumar, Influence of thermomechanical processing parameters on microstructural evolution of a gamma-prime strengthened cobalt based superalloy during high temperature deformation. Materials Science & Engineering A **791**, 139498 (2020). DOI: https://doi.org/10.1016/j.msea-2020-139498

[6] B. Swain, P. Mallick, S. Patel, R. Roshan, S.S. Mohapatra, S. Bhuyan, M. Priyadarshini, B. Behera, S. Samal, A. Behera, Failure analysis and materials development of gas turbine blades. Materials Today: Proceedings **33**, 5143-5146 (2020). DOI: https://doi.org/10.1016/j.matpr-2020-02-859

[7] A.B. Naik, A.C. Reddy, Optimization of tensile strength in TIG welding using the Taguchi method and analysis of variance (ANOVA). Thermal Science and Engineering Progress **8**, 327-339 (2018). DOI: https://doi.org/10.1016/j.tsep-2018-8-5

[8] Y. Xu, G. Fang, N. Lv, S. Chen, J.J. Zou, Computer vision technology for seam tracking in robotic GTAW and GMAW. Robotics and Computer Integrated Manufacturing **32**, 25-36 (2015). DOI: http://dx.doi.org/10.1016/j.rcim-2014-09-002

[9] K. Kumar, C.S. Kumar, M. Masanta, S. Pradhan, A review on TIG welding technology variants and its effect on weld geometry. Materials Today: Proceedings **50**, 999-1004 (2022). DOI: https://doi.org/10.1016/j.matpr-2021-07-308

[10] C. Jiang, X. Wang, X. Xue, Y. Du, W. Wang, Analysis for the welding crack leakage of deethanizer. Journal of Physics: Conference Series **1885**, 032038 (2021). DOI: https://doi.org/10.1088/1742-6596-1885-3-032038

[11] C. Jiang, Y. Du, X. Zhang, W. Pan, Analysis and treatment of cracks in LPG spherical tank. Journal of Physics: Conference Series **1820**, 012065 (2021). DOI: https://doi.org/10.1088/1742-6596-1820-1-012065

[12] B. Wang, B. Lei, W. Wang, M. Xu, L. Wang, Investigations on the crack formation and propagation in the dissimilar pipe welds involving L360QS and N08825. Engineering Failure Analysis **58**, 56-63 (2015). DOI: http://doi.org/10.1016/j.engfailanal-2015-08-034

[13] J.S. Kim, B.Y. Lee, W.G. Hwang, S.S. Kang, T. Zhang, The Effect of Welding Residual Stress for Making Artificial Stress Corrosion Crack in the STS 304 Pipe. Advances in Materials Science and Engineering (2015). DOI: http://doi.org/10.1155-2015-92512

[14] Y. Jun, S. Tian-Min, G. Jian-Jun, Effect of High Temperature Welding on Fatigue Life of 16MnR Joint. Journal of Liaoning Petrochemical University **31**, 25-27 (2011). DOI: http://doi.org/10.3696/j.issn.1672-6952.2011-01-007

[15] I. AghaAli, M. Farzam, M.A. Golozar, I. Danaee, The effect of repeated repair welding on mechanical and corrosion properties of stainless steel 316L. Materials & Design **54**, 331-341 (2014). DOI: https://doi.org/10.1179/136217104225017099

[16] H. Vemanaboina, S. Akella, R.K. Buddu, Welding Process Simulation Model For Temperature and Residual Stress Analysis. Procedia Materials Science **6**, 1539-1546 (2014). DOI: http://doi.org/10.1016/j.mspro-2014-7-135

[17] Zhengyi Wei, Xingjun Gao, Zilong Deng, Lin Fan, Research on Cutting Performance of GH4169 in Ultrasonic Elliptical Vibration Turning Based on ABAQUS. Journal of Liaoning Petrochemical University **41**, 67-71 (2021). DOI: http://doi.org/10.3969/j.issn.1672-6952.2021-06-013

[18] M. Perić, S. Nižetić, I. Garašić, N. Gubeljak, T. Vuherer, Z. Tonković, Numerical calculation and experimental measurement of temperatures and welding residual stresses in a thick-walled T-joint structure. Journal of Thermal Analysis and Calorimetry **141**, 313-322 (2020). DOI: https://doi.org/10.1007/S10973-019-09231-3

[19] R. Sihotang, P. Sung-Sang, B. Eung-Ryul, Effects of heat input on microstructure of tungsten inert gas welding used hastelloy X. Materials Research Innovations **18**, S2-1074-S2-1080 (2014). DOI: https://doi.org/10.1179/1432891714Z-000000000559

[20] L. Zhao, H. Jing, L. Xu, Y. Han, J. Xiu, Analysis of creep crack growth behavior of P92 steel welded joint by experiment and numerical simulation. Materials Science & Engineering A **558**, 119-128 (2012). DOI: http://doi.org/10.1016/j.msea-2012-07-94

[21] Y. Wang, M. Ding, Y. Zheng, S. Liu, W. Wang, Z. Zhang, Finite-Element Thermal Analysis and Grain Growth Behavior of HAZ on Argon Tungsten-Arc Welding of 443 Stainless Steel. Metals **6**, 77 (2016). DOI: https://doi.org/10.3390/met6040077

[22] H. Wang, H.Y. Jing, L. Zhao, Y.D. Han, L.Y. Xu, Study on residual stress in socket weld by numerical simulation and experiment. Science and Technology of Welding and Joining **21**, 504-514 (2016). DOI: http://doi.org/10.1080/13628718-2015-1118812

[23] Y. Rong, J. Xu, Y. Huang, G. Zhang, Review on finite element analysis of welding deformation and residual stress. Science and Technology of Welding and Joining **23**, 198-208 (2018). DOI: http://doi.org/10.1080/13621718-2017-1361673

[24] J. Lee, J. Hwang, D.Bae, Welding Residual Stress Analysis and Fatigue Strength Assessment at Elevated Temperature for Multi-pass Dissimilar Material Weld Between Alloy 617 and P92 Steel. Metals and Materials International **24**, 877-885 (2018). DOI: https://doi.org/10.1007/s12540-018-0086-7

[25] H.R. Abedi, O.A. Ojo, Enhanced resistance to gas tungsten arc weld heat-affected zone cracking in a newly developed Co-based superalloy. Materials Science and Engineering A **851**, 143618 (2022). DOI: https://doi.org/10.1016/j.msea-2022-143618

[26] H.R. Abedi, O.A. Ojo, Numerical Modeling of Gas Tungsten Arc Welding of a Newly Developed Cobalt-Based Superalloy. Metallurgical and Materials Transactions A **52**, 5043-5054 (2021). DOI: https://doi.org/10.1007/s11661-021-06451-x